

Minimum critical velocity of a Gaussian obstacle in a Bose-Einstein condensate

Haneul Kwak,¹ Jong Heum Jung,¹ and Y. Shin^{1,2,3,*}

¹*Department of Physics and Astronomy, Seoul National University, Seoul 08826, Korea*

²*Center for Correlated Electron Systems, Institute for Basic Science, Seoul 08826, Korea*

³*Institute of Applied Physics, Seoul National University, Seoul 08826, Korea*

When a superfluid flows past an obstacle, quantized vortices can be created in the wake above a certain critical velocity. In the experiment by Kwon *et al.* [Phys. Rev. A **91** 053615 (2015)], the critical velocity v_c was measured for atomic Bose-Einstein condensates (BECs) using a moving repulsive Gaussian potential and v_c was minimized when the potential height V_0 of the obstacle was close to the condensate chemical potential μ . Here we numerically investigate the evolution of the critical vortex shedding in a two-dimensional BEC with increasing V_0 and show that the minimum v_c at the critical strength $V_{0c} \approx \mu$ results from the local density reduction and vortex pinning effect of the repulsive obstacle. The spatial distribution of the superflow around the moving obstacle just below v_c is examined. The particle density at the tip of the obstacle decreases as V_0 increases to V_{0c} and at the critical strength, a vortex dipole is suddenly formed and dragged by the moving obstacle, indicating the onset of vortex pinning. The minimum v_c exhibits power-law scaling with the obstacle size σ as $v_c \sim \sigma^{-\gamma}$ with $\gamma \approx 1/2$.

I. INTRODUCTION

A superfluid can flow without friction but only below a certain critical velocity. Above the critical velocity, the superfluid becomes dynamically unstable, generating excitations such as phonons and quantized vortices [1]. Understanding the critical dynamics and critical velocity of a superfluid is of fundamental and practical importance for the study of the transport properties of a superfluid system [2–4]. The key questions are what induces the instability of the superfluid flow and how the energy dissipation evolves with the increasing flow velocity. At substantially high velocities, turbulent states would be developed in the superfluid system with a complex tangle of vortex lines, namely, quantum turbulence [5, 6].

In recent experiments with atomic Bose-Einstein condensates (BECs), a localized optical potential formed by focusing a laser beam was adopted as a movable obstacle [7]. Various superfluid dynamics were investigated by controlling the movement of the obstacle in a sample. From the onset of energy dissipation with increasing obstacle speed, critical velocities of various atomic superfluid gases were demonstrated [7–12], where the measurement results tested theoretical predictions [13–18] and revealed the details of the dissipation mechanisms [9–12, 19, 20]. For a fast obstacle above the critical velocity, the vortex shedding in the wake of the moving obstacle was investigated [21–25]. A remarkable observation was that vortex clusters consisting of like-sign vortices are regularly shed from a uniformly moving obstacle in atomic BECs [22]. This is analogous to the von Kármán vortex street in the classical viscous fluids in the transition to turbulence [24, 25].

For the optical obstacle, there are two regimes with respect to the relative magnitude of the obstacle’s peak

potential V_0 to the chemical potential μ of the BEC. The particle density at the obstacle position is suppressed because of the repulsion of the obstacle. However, when $V_0 < \mu$, the condensate can penetrate the obstacle and a zero-density region is not induced in the condensate. In this penetrable case, vortices can be created only in the form of a dipole consisting of two vortices of opposite circulations. When $V_0 > \mu$, which is referred to as impenetrable, a density-depleted hole is formed in the system, and it would significantly alter the characteristics of the vortex shedding dynamics by allowing the generation of vortex clusters [22]. In the experiment by Kwon *et al.* [9], the critical velocity v_c for vortex shedding was measured as a function of V_0 , and v_c was minimized sharply at a certain critical strength V_{0c} that was close to μ . This implies that the onset behavior of the vortex shedding, which we refer to as critical vortex shedding, undergoes a certain transition as the obstacle strength changes from penetrable to impenetrable.

In this paper, we numerically study the critical vortex shedding of a Gaussian obstacle in a two-dimensional (2D) BEC and investigate its evolution with increasing obstacle strength. We verify that the critical velocity is minimized at a critical obstacle strength V_{0c} close to μ and show that it arises from the start of vortex pinning as V_0 increases above V_{0c} . We examine the spatial distribution of the superflow around the moving obstacle just below v_c . At the critical strength, the superflow distribution suddenly changes to form a vortex dipole that is pinned at the tip of the obstacle. When V_0 is further increased, a density-depleted region develops and the co-moving, pinned vortex dipole becomes virtual and is absorbed in the region. The minimum v_c at $V_0 = V_{0c}$ decreases with increasing the obstacle size σ . We find that it exhibits a power-law scaling of $v_c \sim \sigma^{-\gamma}$, with $\gamma \approx 1/2$, which is in reasonable agreement with the experimental results of Ref. [9]. Our results demonstrate the existence of the minimum critical velocity for a Gaussian obstacle and elucidate the transition of the critical vortex shed-

* yishin@snu.ac.kr

ding from the penetrable to impenetrable regime.

The remainder of this paper is organized as follows. In Sec. II, we describe a theoretical model to study the vortex shedding dynamics in a BEC based on the 2D Gross-Pitaevskii equation. In Sec. III, we present numerical results, including a comparison of the shedding dynamics for penetrable and impenetrable obstacles, and the characterization of the critical vortex dipole state generated by the moving obstacle at the critical strength. Finally, in Sec. IV, a summary of this work and the outlooks for future studies are provided.

II. THEORETICAL MODEL

We consider a situation where an obstacle moves in a homogeneous BEC with a constant velocity \mathbf{v} . In the mean-field theory, the BEC dynamics is described by the Gross-Pitaevskii equation (GPE),

$$i\hbar \frac{\partial \Psi}{\partial t} = \left(-\frac{\hbar^2}{2m} \nabla^2 + V(\mathbf{r} - \mathbf{v}t) + g|\Psi|^2 - \mu \right) \Psi, \quad (1)$$

where $\Psi(\mathbf{r}, t)$ is the macroscopic wave function of the BEC, \hbar is Planck's constant divided by 2π , m is the atom mass, $V(\mathbf{r})$ is the obstacle potential, and g is the nonlinear coupling coefficient. Taking the unitary transformation $\Psi(\mathbf{r}, t) = \exp[-\mathbf{v}t \cdot \nabla] \psi(\mathbf{r}, t)$, Eq. (1) is transformed into the reference frame moving with the obstacle as

$$i\hbar \frac{\partial \psi}{\partial t} = \left(-\frac{\hbar^2}{2m} \nabla^2 + i\hbar \mathbf{v} \cdot \frac{\partial}{\partial \mathbf{x}} + V(\mathbf{r}) + g|\psi|^2 - \mu \right) \psi \quad (2)$$

with $\mathbf{v} = v\hat{\mathbf{x}}$. The characteristic length and time scales of the system are given by the healing length $\xi = \hbar/\sqrt{2m\mu}$ and $t_\mu = \hbar/\mu$, respectively. Using the change in variables, $\tilde{\mathbf{r}} = \mathbf{r}/\xi$ and $\tilde{t} = t/t_\mu$, the equation can be expressed in a dimensionless form as

$$i\partial_{\tilde{t}} \tilde{\psi} = \left(-\tilde{\nabla}^2 + i\sqrt{2}\tilde{v}\partial_{\tilde{x}} + \tilde{V}(\tilde{\mathbf{r}}) + |\tilde{\psi}|^2 - 1 \right) \tilde{\psi} \quad (3)$$

with $\tilde{\psi} = n_0^{-1/2}\psi$, $\tilde{v} = v/c_s$, $\tilde{\nabla} = \xi\nabla$, and $\tilde{V} = V/\mu$. Here $n_0 = \mu/g$ is the particle density of the BEC without the obstacle and $c_s = \sqrt{\mu/m}$ is the speed of sound.

In this work, we study the BEC dynamics for a Gaussian obstacle in two dimensions. This is motivated by the recent experiments using highly oblate atomic samples [9–12, 23], where the vortex line dynamics along the tight confining direction is energetically irrelevant. Hence, the shedding dynamics can be well described in 2D. In a hydrodynamic approximation, the dimensional reduction is carried out by integrating the wave function component along the short axis. It effectively modifies the speed of sound in Eq. (3) [26, 27]. The potential of the Gaussian obstacle is given by $V(r) = V_0 \exp[-2(r^2/\sigma^2)]$, where $r = \sqrt{x^2 + y^2}$ and σ is the $1/e^2$ radius of the obstacle. The obstacle is located at the origin of the reference frame.

We numerically solve Eq. (3) in the xy plane with periodic boundary conditions, using the pseudo spectral method [28]. In the simulation of vortex shedding for $v > v_c$, we set the initial state to be a stationary solution for a velocity v_i slightly below v_c . Next, we increase the obstacle speed up to the target velocity v for an acceleration time $t_a = 200t_\mu$ [29]. The initial stationary solution is obtained using the imaginary-time method where t is replaced by $-i\tau$ [30, 31]. To realize a constant stream at the front boundary of the obstacle, we adopt the numerical method described in Ref. [25], where damping zones with a thickness of 20ξ are set at the boundary to attenuate the wake of the BEC and recover the constant uniform flow at the front boundary. In the calculation of a stationary solution using the imaginary-time propagation method, the damping zone is inactivated.

III. RESULTS AND DISCUSSION

A. Determination of critical velocity

Figures 1(a) and 1(b) display the density distributions of the BEC, $n(x, y) = |\psi|^2$, at $t/t_\mu = 1200$ for two different velocities, $v/c_s = 0.25$ and 0.28 , respectively [29]. The obstacle size and strength are $\sigma/\xi = 20$ and $V_0/\mu = 0.8$. When the speed is lower than the threshold value of $v_c \approx 0.26c_s$, no vortices are generated. The BEC remains stationary [Fig. 1(a)]. By contrast, when the obstacle velocity increases above the threshold velocity, vortices are emitted from the obstacle in a periodic manner [21]. The periodic vortex shedding is also examined by inspecting the drag force exerted by the obstacle $F_x = -\int \tilde{\psi}^* (\partial_{\tilde{x}} \tilde{V}) \tilde{\psi} d^2\tilde{\mathbf{r}}$ using the Ehrenfest relation [25]. We verify that for $v > v_c$ the force oscillates in time, corresponding to the periodic vortex emission. For $v < v_c$ it is stationary and remains approximately zero [Fig. 1(c)].

We determine the critical velocity v_c from the existence of a stationary ground state solution via the imaginary time propagation method [15]. The imaginary time method gives a converging stationary solution for $v < v_c$ or an oscillating solution otherwise. In the oscillating solution, a pair of vortices is created by the obstacle. They move away from each other along the y -direction and are annihilated at the system's boundary due to the periodic boundary conditions. This process is repeated over an imaginary time. In the calculation of stationary solutions, we employed a spatial domain of $(L_x, L_y) = (400, 400)\xi$ with $(N_x, N_y) = (600, 600)$ grids and took a time step of $\Delta\tau/t_\mu = 0.04$. We decided the convergence of a solution through its behavior up to the imaginary time $\tau/t_\mu = 4000$. The critical velocities determined from our imaginary time method are identical to the threshold values from the simulation of the real-time evolution within an error of $0.02c_s$.

Figure 2 displays the numerical results of the critical velocities over a range of obstacle strength $0.1 \leq V_0/\mu \leq$

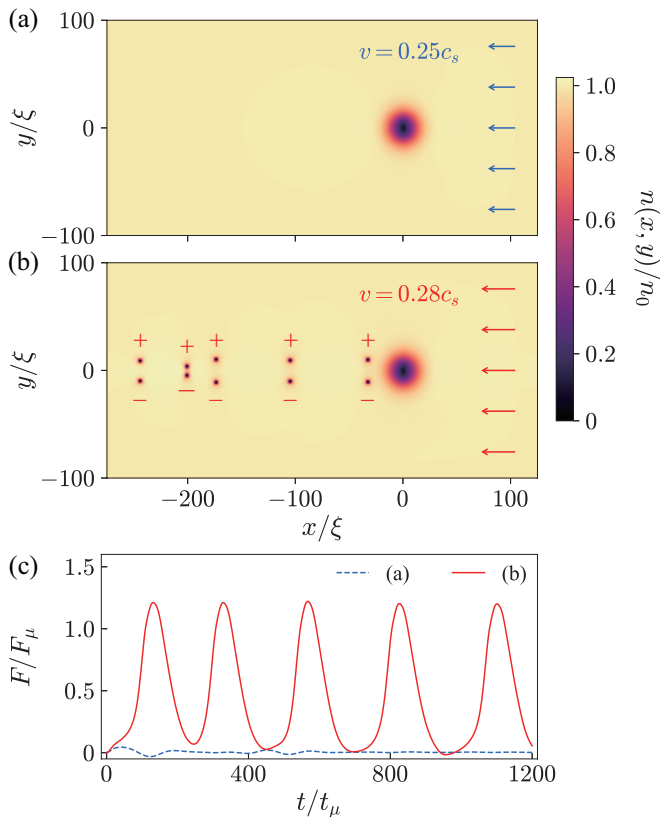


FIG. 1. Vortex shedding from a Gaussian obstacle in a Bose-Einstein condensate. Particle density distribution $n(x, y)$ of a BEC flowing past an obstacle with size $\sigma/\xi = 20$ and strength $V_0/\mu = 0.8$ for flow speed (a) $v/c_s = 0.25$ and (b) 0.28 , at time $t/t_\mu = 1200$. n_0 denotes the particle density of the BEC without the obstacle and the flow direction is indicated by the arrows. In (b), the flow speed is faster than the critical velocity of $v_c \approx 0.26c_s$, and vortices are generated behind the obstacle. The circulation directions of the vortices are indicated by + (counterclockwise) and - (clockwise). (c) Temporal evolution of the drag force F experienced by the BEC in (a) and (b). $F_\mu = \mu/\xi$.

10 for various obstacle radii $4 \leq \sigma/\xi \leq 30$. We observe a marked dip of v_c with a minimum around $V_0 = \mu$, which agrees well with the previous experimental observation [9]. In the limit of $V_0 \rightarrow 0$, v_c approaches to the speed of sound c_s . It is compatible with the fact that the critical velocity of a microscopically small impurity is given by the speed of sound according to the Landau criterion, although such a small obstacle would generate phonons or a localized rarefaction pulse called the Jones-Roberts soliton [32, 33], rather than vortices. In the limit of $V_0 \rightarrow \infty$, the Gaussian obstacle is well represented as a hard cylinder. v_c is expected to converge to a constant value of approximately $0.4c_s$. It was verified numerically [15] and analytically [16] that the critical velocity of a large hard cylinder is given by $\approx 0.37c_s$ regardless of the diameter of the cylinder.

The local Landau criterion provides a qualitative interpretation of the observed V_0 dependence of v_c . Namely,

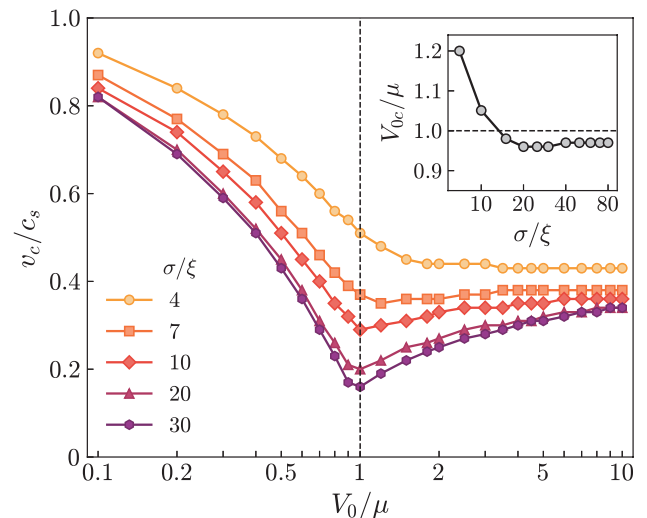


FIG. 2. Critical velocity v_c as a function of the obstacle strength V_0 for various obstacle sizes σ . The x -axis has a logarithmic scale. For $\sigma/\xi > 4$, v_c is minimized at a critical strength V_{0c} , close to the chemical potential μ of the BEC. The dashed line denotes $V_0 = \mu$ and represents the boundary between the penetrable regime and the impenetrable regime. The inset shows the critical obstacle strength V_{0c} as a function of σ .

when $V_0 < \mu$, the particle density in the obstacle region decreases with an increasing V_0 as $n \approx (\mu - V_0)/g$. This lowers the local speed of sound at the tip of the obstacle and consequently, decreases the critical velocity. However, when $V_0 > \mu$, a density-depleted region is formed by the obstacle. Vortices would be generated at the flanks of the obstacle, restoring v_c to that in the hard cylinder case. However, it is not clear why the critical velocity sharply changes its behavior at the critical obstacle strength $V_{0c} \approx \mu$. In addition, when the obstacle size is reduced below 10ξ , the critical obstacle strength of the minimum v_c is slightly shifted to a higher V_0 . Eventually, for $\sigma/\xi < 7$ the local minimum of v_c does not occur in our investigation range of V_0 . The inset in Fig. 2 shows V_{0c} as a function of σ . The main purpose of this work is to probe the underlying mechanism of the minimum v_c at the critical obstacle strength.

B. Penetrable-to-impenetrable transition

We first compare the characteristics of the vortex generation dynamics for penetrable and impenetrable obstacles. In Fig. 3, we display a time sequence of the phase and velocity field distributions around the obstacle as vortices are generated for the two cases with $V_0/\mu = 0.8$ and 3.0 , respectively. The velocity field of a superfluid is determined from the probability current $\mathbf{j} = -\frac{i\hbar}{2m}(\psi^*\nabla\psi - \psi\nabla\psi^*) = \frac{\hbar}{m}|\psi|^2\nabla\Phi \equiv n\mathbf{v}_s$ with $\Phi(\mathbf{r})$ being the phase of the macroscopic wave function $\psi(\mathbf{r})$.

For the penetrable obstacle, two zero-velocity regions,

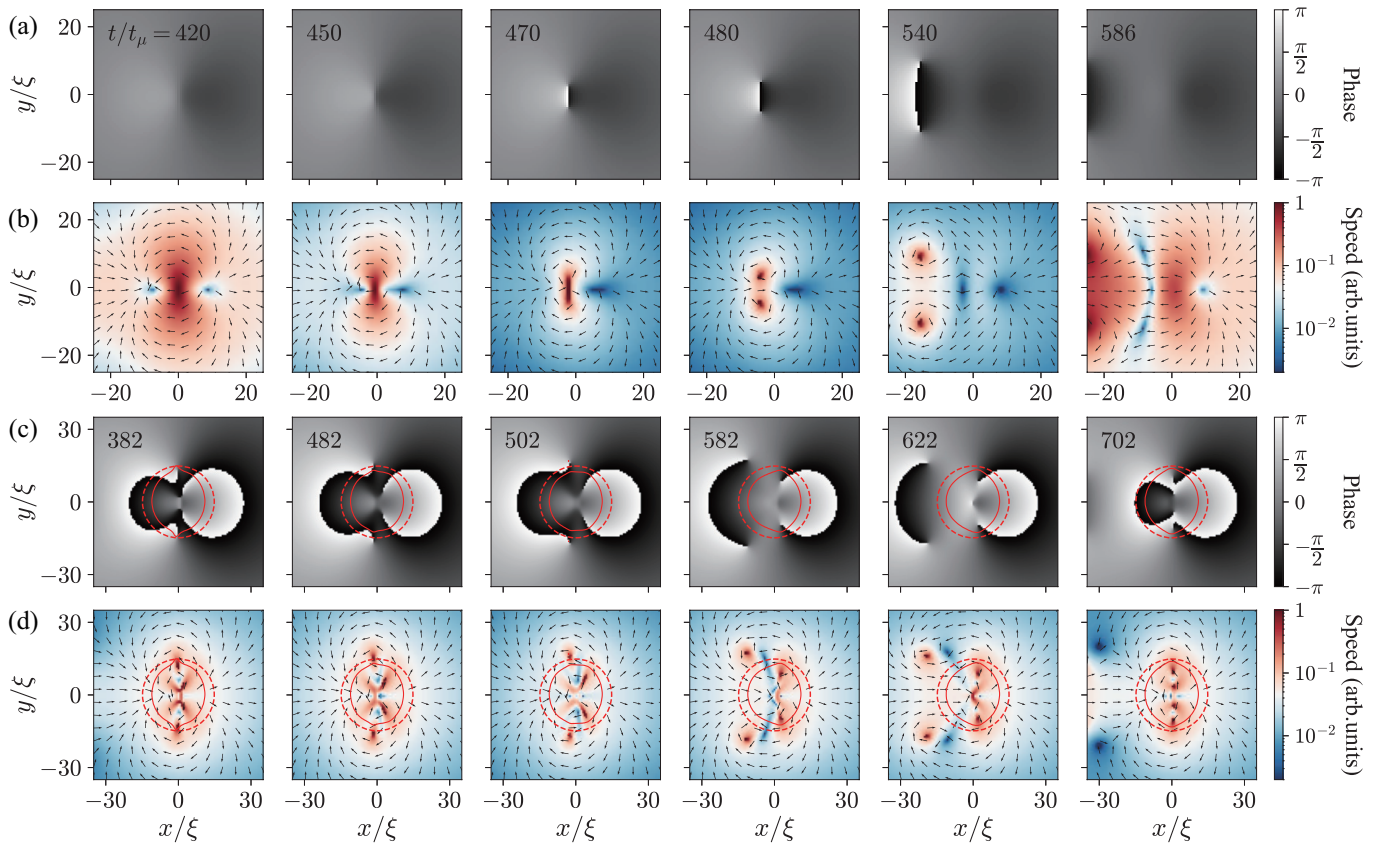


FIG. 3. Vortex nucleation process. Time evolution of the phase (a,c) and velocity field (b,d) of a BEC for a penetrable obstacle ($\sigma/\xi = 20$, $V_0/\mu = 0.8$, $v/c_s = 0.27$) in (a) and (b), and for an impenetrable obstacle ($\sigma/\xi = 20$, $V_0/\mu = 3.0$, $v/c_s = 0.30$) in (c) and (d). In (b) and (d), the flow speed is normalized with the maximum speed in each panel. In (c) and (d), the red dashed circles delineate the boundary of the region where the obstacle's repulsive potential is larger than the chemical potential μ of the BEC. The red solid lines indicate the particle-density contour line at 0.1% of n_0 . The velocity field in the zero-density region is virtual.

indicated by the dark blue area in Fig. 3(b), are formed at the front and rear of the obstacle, respectively, and they have a high velocity region between them. The mass flow diverges out in the front region and converges behind the obstacle. This is a consequence of the pressure increase at the front and the subsequent pressure drop behind the moving obstacle. As time passes, the rear zero-velocity region gradually disappears and the high-velocity area evolves into a vortex pair separated along the y direction. At the vortex nucleation moment, the flow direction in the high-velocity region is rapidly flipped due to the phase accumulation and slippage [14, 34]. As the vortex dipole is shed, the front zero-velocity region is separated into two parts along the obstacle's moving direction. The same vortex dipole generation process is repeated.

For the impenetrable obstacle case of $V_0/\mu = 3$, two pairs of vortices exist inside a density-depleted region [Figs. 3(c) and 3(d)]. These virtual vortices correspond to the superflow pattern around the obstacle. Vortex emission occurs by peeling off the two outer vortices into the condensate. The remaining two vortices inside the

density-depleted zone come out to the obstacle's boundary and simultaneously, a new vortex pair is produced at the center of the obstacle. It forms a configuration identical to that before the vortex emission, thus preparing for the next emission. This vortex emission via unpinning from the obstacle's boundary layer is qualitatively different from that for the penetrable obstacle, where a vortex dipole is generated via phase slippage at the tip of the obstacle.

To investigate the evolution of the critical vortex shedding with an increasing V_0 , in Fig. 4 we display the phase and velocity fields of the stationary solutions at $v \rightarrow v_c^-$, for $\sigma/\xi = 20$ and various V_0 . In the penetrable regime, as V_0 increases to V_{0c} , the two zero-velocity regions get closer and the in-between high-velocity region becomes more localized. At the critical potential strength $V_{0c} \approx \mu$, the obstacle creates phase discontinuity [Fig. 4(b)]. Subsequently, a pair of vortices, which are pinned, i.e., stationary with the obstacle, appear [Fig. 4(c)]. A density-depleted region is not formed yet at the center of the obstacle even for $V_0/\mu = 1.2$ [Fig. 4(d)]. As V_0 increases further, a zero-density region develops and eventually, for

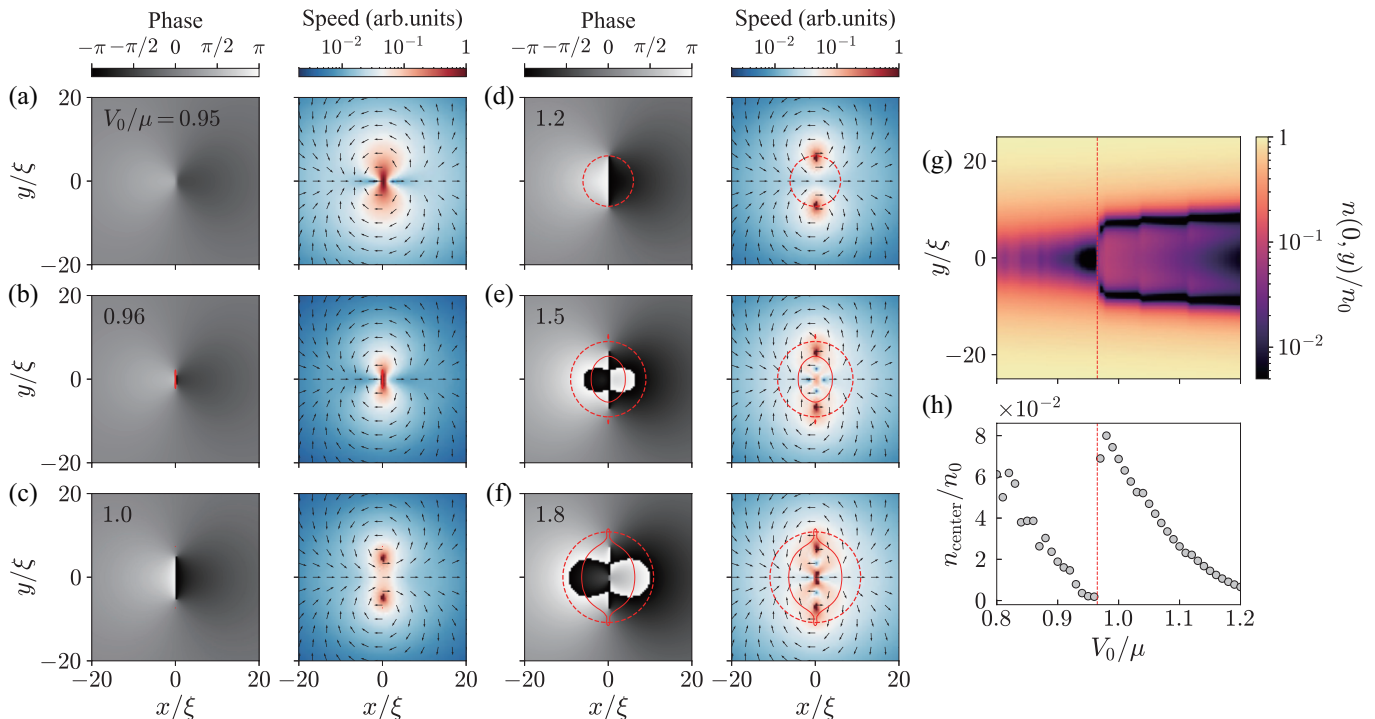


FIG. 4. Penetrable-to-impenetrable transition of the critical superflow around the moving Gaussian obstacle. (a–f) Spatial distributions of the phase (left) and velocity field (right) of a BEC for various obstacle strengths (a) $V_0/\mu = 0.95$, (b) 0.96, (c) 1.0, (d) 1.2, (e) 1.5, and (f) 1.8, where $\sigma/\xi = 20$. The obstacle velocity is $v \rightarrow v^-$, i.e., just below v_c for each obstacle strength. The colormap and red dashed and solid lines have the same meaning as in Fig. 3. (g) Particle density profile $n(0, y)$ of the BEC at the critical velocity as a function of V_0 . The colorbar has a logarithmic scale. Just above the critical strength $V_{0c} = 0.96\mu$, the density minimum is bifurcated, corresponding to the vortex dipole formation. (h) The density n_{center} at the center of the obstacle is shown as a function of V_0 , which corresponds to the horizontal line of $y = 0$ in (g). The red dashed lines in (g,h) mark the critical strength V_{0c} .

$V_0/\mu > 1.5$, the pinned vortex dipole is absorbed in the density-depleted region and becomes virtual [Fig. 4(e)]. For even higher V_0 , a new bound virtual vortex pair appears in the zero-density region [Fig. 4(f)]. The evolution of the superflow pattern at the critical condition shows that the sudden formation of a vortex dipole pinned at the tip of the obstacle represents the transition of the critical vortex shedding from the penetrable to impenetrable regime.

The transition at the critical strength is also demonstrated in the evolution of the particle density profile along $x = 0$ [Fig. 4(g)]. As the obstacle strength increases in the penetrable regime, the density n_{center} at the obstacle's tip decreases to zero as V_0 approaches V_{0c} . When V_0 exceeds V_{0c} , the BEC does not develop a density-depleted region at the tip of the obstacle. Instead, it creates a vortex pair, which is indicated by a bifurcation of the zero-density point in the density profile. Correspondingly, at the tip of the obstacle, n_{center} shows a sudden jump [Fig. 4(h)]. As a result, even if the obstacle height is higher than the chemical potential, n_{center} remains finite.

The formation of a vortex dipole at $V_0 > V_{0c}$ indicates the onset of the pinning effect from the repulsive obstacle. The pinning effect is checked by the fact that the bare linear velocity of the vortex pair, which is given

by $v_d = \frac{\hbar}{md}$ with separation d [35], is smaller than the obstacle velocity. The Magnus force exerted on the vortices points outside of the obstacle [36]. Thus, the vortex dipole is dragged by the moving obstacle under the pinning. The vortex pinning effect makes vortex shedding difficult. Therefore, we attribute the sudden increase of v_c when V_0 increases above V_{0c} to the activation of the vortex pinning effect. Recently, in Ref. [37], the vortex pinning mechanisms were numerically investigated for a circular, uniform potential, and a similar stationary solution was reported.

The onset of the vortex pinning effect explains the observation in Fig. 2 that for small obstacles, V_{0c} is shifted towards a higher value and it disappears at $\sigma/\xi < 7$. Due to the finite size of a vortex core, for sufficiently small obstacles, a vortex dipole with separate cores could not be stably produced in a pinned configuration and thus, v_c monotonically decreases with increasing V_0 . We label such a small obstacle as a *quantum obstacle* [25]. In general, strong impenetrable obstacles would generate vortex clusters, which consist of many same-sign vortices, for high velocity. However, lacking the pinning effect, a quantum obstacle would not lead to large vortex cluster shedding even for high V_0 [25]. Some numerical results are presented in the Appendix.

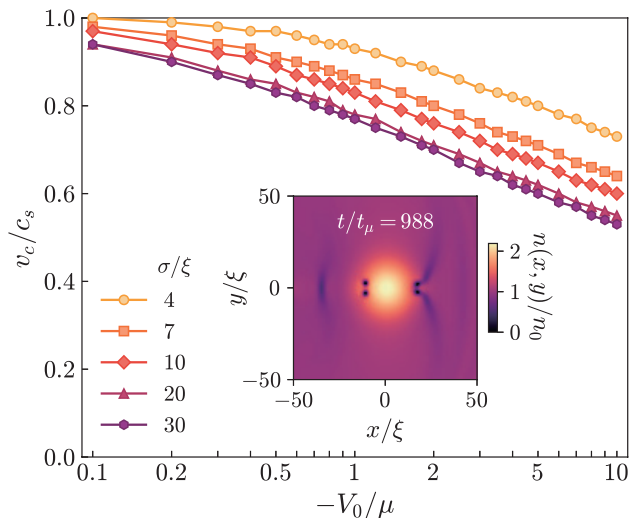


FIG. 5. Critical velocities for various attractive obstacles. The x -axis has a logarithmic scale. The inset shows the particle density distribution $n(x, y)$ of a BEC flowing past an attractive obstacle with $\sigma/\xi = 20$ and $V_0/\mu = -1$, where the obstacle is is accelerated from $0.7c_s$ to $0.85c_s$ for a time of $1000t_\mu$.

Finally, for completeness, we calculate the critical velocities for attractive obstacles with negative V_0 and present the results in Fig. 5. As $|V_0|$ increases, the critical velocity monotonically decreases. The inset in Fig. 5 shows the vortex creation process from an attractive obstacle, where a vortex dipole is generated from a rarefaction pulse being broken in front of the obstacle [38, 39].

C. Obstacle size dependence

In the study of the critical velocity of superflow past an obstacle, the dependence of v_c on the obstacle size has attracted interest because it may reflect the dispersion property of the excitation mode involved in the critical energy dissipation [18, 40]. In our situation with a Gaussian obstacle, we observe that the variations of v_c around $V_0 = \mu$ becomes more pronounced for a larger σ with lowering the minimum v_c (Fig. 2).

Figure 6(a) displays the minimum critical velocity v_{c0} at $V_0 = V_{0c}$ as a function of the obstacle radius σ in a log-log scale, together with the experimental measurement data from Ref. [9]. First, our numerical results are in good quantitative agreement with the experimental results [41]. Second, they suggest a power-law dependence of v_{c0} on σ . From a power-law function of $v_{c0} = v_0(\sigma/\xi)^{-\gamma}$ fitted to the data points, we obtain $\{v_0/c_s, \gamma\} = \{1.19(3), 0.61(1)\}$ for the numerical results and $\{2.3(7), 0.78(9)\}$ for the experimental data.

To understand the origin of the scaling behavior, we consider the GPE for $V_0 = \mu$ in the large obstacle limit, $\sigma \gg \xi$, and in the obstacle center region, where the obstacle potential is approximated as $V(\mathbf{r}) \approx \mu[1 - 2(r/\sigma)^2]$.

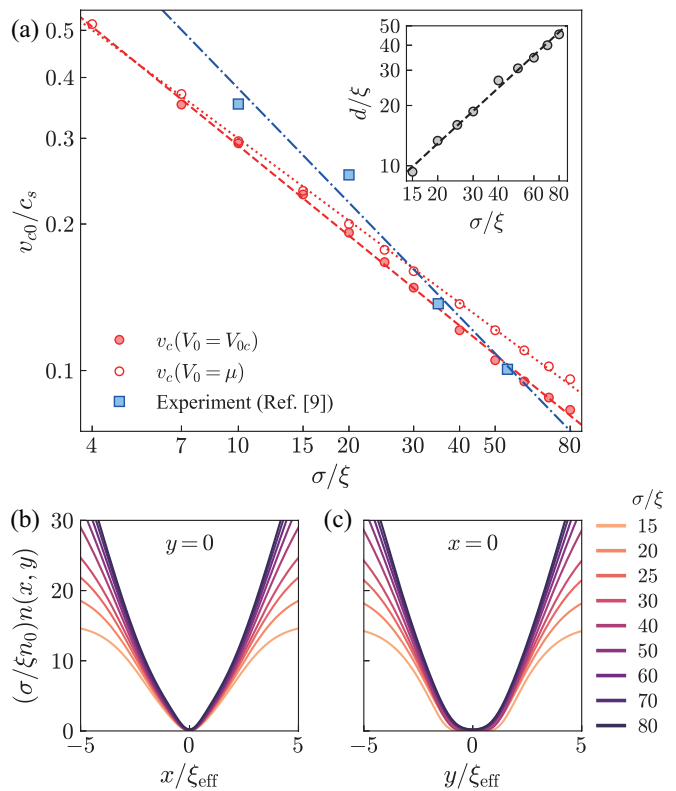


FIG. 6. Obstacle size dependence of the critical velocity. (a) Minimum critical velocity v_{c0} (red solid circles) and v_c at $V_0 = \mu$ (red open circles) as functions of σ . The blue squares are the experimental results from Ref. [9]. All data are plotted in log-log scale. The lines are power-law functions of $v_c = v_0(\sigma/\xi)^{-\gamma}$, fitted to the data sets with $\{v_0/c_s, \gamma\} = \{1.19, 0.61\}$ for the minimum v_c , $\{1.09, 0.56\}$ for v_c at $V_0 = \mu$, and $\{2.3, 0.78\}$ for the experimental data. The inset displays the pair separation d of the critical vortex dipole as a function of σ at $V_0 = \mu$. The black dashed line is a power-law function fit to the data, yielding $d = d_0(\sigma/\xi)^{\gamma_d}$ with $d_0 = 0.81\xi$ and $\gamma_d = 0.92$. Rescaled particle density profiles along (b) $y = 0$ and (c) $x = 0$ at $v \rightarrow v_c^-$ and $V_0 \rightarrow V_{0c}^-$ for various obstacle sizes.

Expecting a scaling behavior of the critical superflow state with σ , we introduce new length and time scales as $\xi_{\text{eff}} = \xi s^\alpha$ and $t_{\mu, \text{eff}} = t_\mu s^\beta$ with $s = \sigma/\xi$, respectively. By changing the variables, $\bar{\mathbf{r}} = \mathbf{r}/\xi_{\text{eff}}$ and $\bar{t} = t/t_{\mu, \text{eff}}$, we obtain a dimensionless expression for the GPE, which is explicitly independent of σ . When $\alpha = \frac{1}{2}$ and $\beta = 1$, Eq. (2) is recaptured in a σ -independent form as

$$i\partial_{\bar{t}}\bar{\psi} = \left(-\bar{\nabla}^2 + i\sqrt{2}\bar{v}\partial_{\bar{x}} - 2\bar{r}^2 + |\bar{\psi}|^2\right)\bar{\psi}, \quad (4)$$

where $\bar{v} = s^{1/2}(v/c_s)$, $\bar{\nabla} = \xi_{\text{eff}}\nabla$, and $\bar{\psi} = (n_0/s)^{-1/2}\psi$. This suggests that $v_c \propto 1/\sqrt{\sigma}$, which is close to the observed scaling behavior of the minimum critical velocity v_{c0} with σ . Noting that V_{0c} is not exactly equal to μ , in Fig. 6(a), we also plot v_c at $V_0 = \mu$ (red open circles) as a function of σ . A power-law fitting gives $\{v_0/c_s, \gamma\} = \{1.09(2), 0.56(1)\}$. It agrees better with the

prediction of Eq. (4). The power-law relation estimates the critical velocity with considerable accuracy throughout the whole range of σ including the quantum obstacle regime.

The dimensionless GPE of Eq. (4) suggests the characteristic length scale of the system $\xi_{\text{eff}} = \sqrt{\xi\sigma}$. In Figs. 6(b) and 6(c), we plot the profiles of normalized particle density $\bar{n} = |\bar{\psi}|^2 = \frac{1}{n_0} \frac{\xi_{\text{eff}}^2}{\xi^2} |\psi|^2$ along $y = 0$ and $x = 0$, respectively, for various σ , where the wave functions $\psi(\mathbf{r})$ for the critical condition of $V_0 \rightarrow V_{0c}^-$ and $v \rightarrow v_{c0}^-$ are calculated from Eq. (2). The normalized number densities collapse remarkably well in the center region of $r \ll \sigma$ as expected from Eq. (4). The length scale ξ_{eff} may be regarded as an effective healing length for the average condensate density $\langle n \rangle$ in the obstacle center region, i.e., $\xi_{\text{eff}} = \hbar/\sqrt{2mg\langle n \rangle}$. Here, $\langle n \rangle$ is estimated in a self-consistent manner as $\langle n \rangle = \frac{1}{\pi\xi_{\text{eff}}^2} \int_{r < \xi_{\text{eff}}} n(\mathbf{r}) d^2\mathbf{r}$. It is the mean value over a disk area of radius ξ_{eff} . With $n(r) = n_0 \frac{2r^2}{\sigma^2}$ for $r \ll \sigma$, $\langle n \rangle = n_0 \frac{\xi_{\text{eff}}^2}{\sigma^2}$, yielding $\xi_{\text{eff}} = \sqrt{\xi\sigma}$.

Finally, we investigate the dependence of the pair separation d of the critical vortex dipole state on the obstacle size. In the inset of Fig. 6(a), the pair separation d at $V_0 = \mu$ is plotted as a function of σ in a log-log scale, and we observe that d exhibits power-law scaling with σ as $d \propto \sigma^{0.9}$. The scaling exponent is not accounted for by the length scale ξ_{eff} , which is understandable because the vortex separation is the order of the obstacle radius, invalidating the center-region approximation in Eq. (4).

According to Ref. [36, 37], the velocity of a vortex is given by

$$\mathbf{v}_v = \frac{\hbar}{m} \left(\nabla\Phi - \frac{1}{2} \hat{\mathbf{k}} \times \nabla \ln n \right) \Big|_{\mathbf{r}_v}, \quad (5)$$

where \mathbf{r}_v denotes the vortex position and $\hat{\mathbf{k}}$ is the circulation direction of the vortex. The first term describes a velocity from the ambient phase gradient without the vortex's singular contribution. The second term describes the one induced from the density gradient. In the critical vortex dipole state, assuming that the vortices generate a phase gradient equal to that in a homogeneous BEC, the first term arising from the counterpart vortex in the dipole is estimated as $\frac{\hbar}{m} \nabla\Phi \sim \frac{\hbar}{md} \hat{\mathbf{x}}$. Taking $n(r) = n_0(1 - e^{-2\frac{r^2}{\sigma^2}})$ in the Thomas-Fermi approximation, the second term gives $v_d = -\frac{\hbar}{m} \hat{\mathbf{z}} \times \nabla \ln n = \frac{\hbar}{m} \frac{n_0 - n(\frac{d}{2})}{n(\frac{d}{2})} \frac{d}{\sigma^2} \hat{\mathbf{x}}$. Then, from $\mathbf{v}_v = v_c \hat{\mathbf{x}}$, the observation of $d \sim \sigma$ suggests $v_c \sim 1/\sigma$, which is not compatible with the observed scaling behavior of v_c . This implies that the velocity field around the vortex dipole is significantly modified in the inhomogeneous density distribution due to the obstacle potential [42]. The structure and stability of the critical vortex dipole state are an interesting subject and warrants further investigation in future.

IV. SUMMARY AND OUTLOOK

We numerically investigated the critical velocity of a Gaussian obstacle in a uniform 2D BEC using the GPE. From the existence of a stationary solution, we determined the critical velocity as a function of the obstacle strength. It is minimized at the critical strength $V_{0c} \approx \mu$, which is consistent with the previous experimental results in Ref. [9]. We examined the flow pattern of the condensate around the obstacle for the velocity just below v_c . A vortex dipole is abruptly formed at the tip of the obstacle as the obstacle strength exceeds V_{0c} . This sudden change in the critical flow pattern indicates the onset of the vortex pinning effect by the moving obstacle. It represents the penetrable-to-impenetrable transition of the vortex shedding dynamics. Further, the minimum critical velocity at the critical obstacle strength exhibits a power-law dependence on the obstacle size as $v_c \propto \sigma^{-\gamma}$ with $\gamma \approx 1/2$. Additionally, the measured exponent is explained by the scaling property of the GPE near the center of the obstacle with $V_0 = \mu$.

The superflow state where a vortex dipole is pinned and dragged by the moving obstacle presents an interesting situation for the study of the critical vortex shedding. As mentioned in the discussion of the σ dependencies of v_c and d , the structure of the critical vortex dipole state and its stability need to be further investigated. A force balance analysis including the Magnus force and vortex attraction in the background with inhomogeneous density might be fruitful [36, 42, 43]. Near the critical shedding condition, small breathing motions of the vortex dipole were observed in our numerical simulation, where acoustic radiation from the vortex dipole-obstacle interaction is anticipated [44]. At the critical obstacle strength, the transition of the superflow distribution appears very rapid, similar to the first-order. Thus, it suggests that there might be some hysteresis effects in the vortex shedding when the obstacle changes its strength in time. In Ref. [45], the bistability in the vortex shedding near the critical velocity was reported. Lastly, the recent experimental work on the vortex shedding frequency f_v showed that the increasing rate of f_v with the obstacle velocity is fastest at $V_0 \approx \mu$ [23]. This might have originated from the critical vortex dipole state at the critical obstacle strength.

ACKNOWLEDGMENTS

This work was supported by the National Research Foundation of Korea (NRF-2018R1A2B3003373, NRF-2019M3E4A1080400) and the Institute for Basic Science in Korea (IBS-R009-D1).

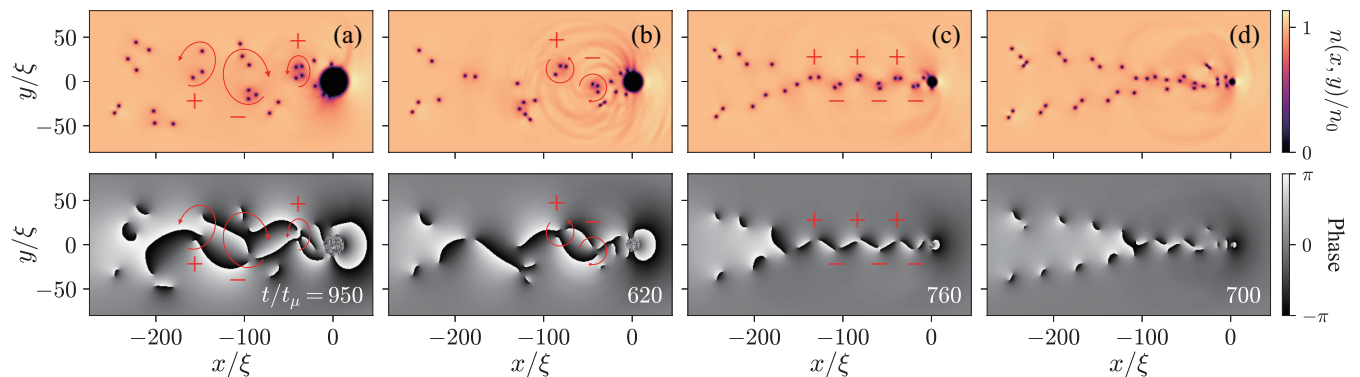


FIG. 7. Vortex cluster shedding for strong impenetrable obstacles. The particle density (top) and phase (bottom) distributions of a BEC flowing past a strong impenetrable obstacle with $V_0/\mu = 100$: (a) $\sigma/\xi = 10$, (b) 7, (c) 3.5, and (d) 2. The obstacles were accelerated from $0.35c_s$ to $0.525c_s$ in (a), from $0.4c_s$ to $0.6c_s$ in (b,c), and from $0.45c_s$ to $0.575c_s$ in (d) for $1000t_\mu$. The circulation direction of each vortex cluster is indicated by the red arrow and sign.

Appendix A: Vortex cluster shedding

When an impenetrable obstacle moves at high velocity above v_c , it can generate vortex clusters consisting of many same-sign vortices [25] due to its ability to pin multiple vortices. In Fig. 7, we present numerical results of the vortex cluster shedding for various obstacle sizes. In the numerical simulations, small Gaussian noises are added to the initial wave function of the BEC [24], which break the left-right symmetry of the system with respect to the obstacle moving direction and facilitate the al-

ternate shedding of vortex clusters with different signs of net circulation via hydrodynamic instability. The obstacle is accelerated up to above $0.5c_s$. The size of the vortex clusters decreases with decreasing obstacle size. For obstacles with further reduced radii of $\sigma/\xi_s < 4$, von Kármán streets of same-signed vortex pairs are observed [Figs. 7(c) and 7(d)] [24]. In Fig. 7(d) for our smallest obstacle, we observe that the distances between the vortex clusters are reduced and the Kármán street structure collapses due to the interactions between adjacent clusters.

-
- [1] L. D. Landau, Theory of the superfluidity of helium II, *J. Phys. USSR* **5**, 71 (1941).
 - [2] P. W. Anderson, Considerations on the flow of superfluid helium, *Rev. Mod. Phys.* **38**, 298 (1966).
 - [3] G. Blatter, M. V. Feigel'man, V. B. Geshkenbein, A. I. Larkin, and V. M. Vinokur, Vortices in high-temperature superconductors, *Rev. Mod. Phys.* **66**, 1125 (1994).
 - [4] E. Varoquaux, Anderson's considerations on the flow of superfluid helium: Some offshoots, *Rev. Mod. Phys.* **87**, 803 (2015).
 - [5] W. F. Vinen and J. J. Niemela, Quantum turbulence, *J. Low Temp. Phys.* **128**, 167 (2002).
 - [6] A. C. White, B. P. Anderson, and V. S. Bagnato, Vortices and turbulence in trapped atomic condensates, *Proc. Natl. Acad. Sci. U.S.A.* **111**, 4719 (2014).
 - [7] C. Raman, M. Köhl, R. Onofrio, D. S. Durfee, C. E. Kulewicz, Z. Hadzibabic, and W. Ketterle, Evidence for a Critical Velocity in a Bose-Einstein Condensed Gas, *Phys. Rev. Lett.* **83**, 2502 (1999).
 - [8] R. Desbuquois, L. Chomaz, T. Yefsah, J. Léonard, J. Beugnon, C. Weitenberg, and J. Dalibard, Superfluid behaviour of a two-dimensional Bose gas, *Nat. Phys.* **8**, 645 (2012).
 - [9] W. J. Kwon, G. Moon, S. W. Seo, and Y. Shin, Critical velocity for vortex shedding in a Bose-Einstein condensate, *Phys. Rev. A* **91**, 053615 (2015).
 - [10] W. Weimer, K. Morgener, V. P. Singh, J. Siegl, K. Hueck, N. Luick, L. Mathey, and H. Moritz, Critical Velocity in the BEC-BCS Crossover, *Phys. Rev. Lett.* **114**, 095301 (2015).
 - [11] J. W. Park, B. Ko, and Y. Shin, Critical Vortex Shedding in a Strongly Interacting Fermionic Superfluid, *Phys. Rev. Lett.* **121**, 225301 (2018).
 - [12] J. H. Kim, D. Hong, K. Lee and Y. Shin, Critical Energy Dissipation in a Binary Superfluid Gas by a Moving Magnetic Obstacle, *Phys. Rev. Lett.* **127**, 095302 (2021).
 - [13] T. Frisch, Y. Pomeau, and S. Rica, Transition to Dissipation in a Model of Superflow, *Phys. Rev. Lett.* **69**, 1644 (1992).
 - [14] B. Jackson, J. F. McCann, and C. S. Adams, Vortex Formation in Dilute Inhomogeneous Bose-Einstein Condensates, *Phys. Rev. Lett.* **80**, 3903 (1998).
 - [15] C. Huepe and M. E. Brachet, Scaling laws for vortical nucleation solutions in a model of superflow, *Phys. D (Amsterdam, Neth.)*, **140**, 126-140, (2000).
 - [16] S. Rica, A remark on the critical speed for vortex nucleation in the nonlinear Schrödinger equation, *Phys. D (Amsterdam, Neth.)*, **148**, 221-226, (2001).
 - [17] M. Crescimanno, C. G. Koay, R. Peterson, and R. Walsworth, Analytical estimate of the critical velocity for vortex pair creation in trapped Bose condensates, *Phys. Rev. A* **62**, 063612 (2000).

- [18] J. S. Stieflinger and W. Zwerger, Critical velocity of superfluid flow past large obstacles in Bose-Einstein condensates, *Phys. Rev. A* **62**, 061601(R) (2000).
- [19] V. P. Singh, W. Weimer, K. Morgener, J. Siegl, K. Hueck, N. Luick, H. Moritz, and L. Mathey, Probing superfluidity of Bose-Einstein condensates via laser stirring, *Phys. Rev. A* **93**, 023634 (2016).
- [20] V. P. Singh, C. Weitenberg, J. Dalibard, and L. Mathey, Superfluidity and relaxation dynamics of a laser-stirred two-dimensional Bose gas, *Phys. Rev. A* **95**, 043631 (2017).
- [21] W. J. Kwon, S. W. Seo, and Y. Shin, Periodic shedding of vortex dipoles from a moving penetrable obstacle in a Bose-Einstein condensate, *Phys. Rev. A* **92**, 033613 (2015).
- [22] W. J. Kwon, J. H. Kim, S. W. Seo, and Y. Shin, Observation of von Kármán Vortex Street in an Atomic Superfluid Gas, *Phys. Rev. Lett.* **117**, 245301 (2016).
- [23] Y. Lim, Y. Lee, J. Goo, D. Bae, and Y. Shin, Vortex shedding frequency of a moving obstacle in a Bose-Einstein condensate, *New J. Phys.* **24**, 083020 (2022).
- [24] K. Sasaki, N. Suzuki, and H. Saito, Bénard–von Kármán Vortex Street in a Bose-Einstein Condensate, *Phys. Rev. Lett.* **104**, 150404 (2010).
- [25] M. T. Reeves, T. P. Billam, B. P. Anderson, and A. S. Bradley, Identifying a Superfluid Reynolds Number via Dynamical Similarity, *Phys. Rev. Lett.* **114**, 155302 (2015).
- [26] S. Stringari, Dynamics of Bose-Einstein condensed gases in highly deformed traps, *Phys. Rev. A* **58**, 2385 (1998).
- [27] J. H. Kim, D. H. Hong, and Y. Shin, Observation of two sound modes in a binary superfluid gas, *Phys. Rev. A* **101**, 061601(R) (2020).
- [28] X. Antoine and R. Duboscq, GPELab, a Matlab toolbox to solve Gross–Pitaevskii equations II: Dynamics and stochastic simulations, *Comput. Phys. Commun.* **193**, 95–117 (2015).
- [29] For real-time evolution, we use a spatial domain of $(L_x, L_y) = (400, 200)\xi$ with $(N_x, N_y) = (600, 300)$ equally distributed grids to simulate the periodic vortex shedding. The time interval is set by $\Delta t/t_\mu = 0.04$.
- [30] F. Dalfovo and S. Stringari, Bosons in anisotropic traps: Ground state and vortices, *Phys. Rev. A* **53**, 2477 (1996).
- [31] M. L. Chiofalo, S. Succi, and M. P. Tosi, Ground state of trapped interacting Bose-Einstein condensates by an explicit imaginary-time algorithm, *Phys. Rev. E* **62**, 7438 (2000).
- [32] C. A. Jones, S. J. Putterman, and P. H. Roberts, Motions in a Bose condensate. V. Stability of solitary wave solutions of non-linear Schrodinger equations in two and three dimensions, *J. Phys. A* **19**, 2991 (1986).
- [33] N. Meyer, H. Proud, M. Perea-Ortiz, C. O’Neale, M. Baumert, M. Holynski, J. Kronjäger, G. Barontini, and K. Bongs, Observation of Two-Dimensional Localized Jones-Roberts Solitons in Bose-Einstein Condensate, *Phys. Rev. Lett.* **119**, 150403 (2017).
- [34] In the velocity field calculation, if two adjacent coordinates have a phase difference above 85% of 2π , we subtract 2π from the original phase difference so to realize the inversion of the flow direction.
- [35] M. M. Cawte, X. Yu, B. Anderson, and A. Bradley, Snell’s Law for a vortex dipole in a Bose-Einstein condensate, *SciPost Phys.*, **6**, 032 (2019).
- [36] A. J. Groszek, D. M. Paganin, K. Helmerson and T. P. Simula, Motion of vortices in inhomogeneous Bose-Einstein condensates, *Phys. Rev. A* **97**, 023617 (2018).
- [37] O. R. Stockdale, M. T. Reeves, and M. J. Davis, Dynamical Mechanisms of Vortex Pinning in Superfluid Thin Films, *Phys. Rev. Lett.* **127**, 255302 (2021).
- [38] B. Jackson, J. F. McCann, and C. S. Adams, Dissipation and vortex creation in Bose-Einstein condensed gases, *Phys. Rev. A* **61**, 051603(R) (2000).
- [39] T. Aioi, T. Kadokura, T. Kishimoto, and H. Saito, Controlled Generation and Manipulation of Vortex Dipoles in a Bose-Einstein Condensate, *Phys. Rev. X* **1**, 021003 (2011).
- [40] R. P. Feynman, Chapter II Application of quantum mechanics to liquid helium, *Prog. Low Temp. Phys.* **1**, 17 (1955).
- [41] In Ref. [9], the speed of sound was estimated for the peak atomic density of the trapped condensate.
- [42] D. E. Sheehy and L. Radzihovsky, Vortices in spatially inhomogeneous superfluids, *Phys. Rev. A*, **70**, 063620 (2004).
- [43] L. Thompson, Equation of motion of a quantum vortex (Ph.D. dissertation, University of British Columbia) (2010).
- [44] K. Suthar, A. Roy, and D. Angom, Acoustic radiation from vortex-barrier interaction in atomic Bose-Einstein condensate, *J. Phys. B* **47**, 135301 (2014).
- [45] T. Kadokura, J. Yoshida, and H. Saito, Hysteresis in quantized vortex shedding, *Phys. Rev. A*, **90**, 013612 (2014).